Performance of the RuO2 Catalyst Layer with Nonuniform Ionomer Distribution for Water Electrolysis

Peer-reviewed author version

PAUL, Subir; HARDY, An; SAFARI, Momo & VANDEWAL, Koen (2025)
Performance of the RuO2 Catalyst Layer with Nonuniform Ionomer Distribution for
Water Electrolysis. In: Energy & fuels, 39 (46) , p. 22387 -22397.

DOI: 10.1021/acs.energyfuels.5c04530
Handle: http://hdl.handle.net/1942/47851

Performance of RuO_2 catalyst layer with non-uniform ionomer distribution for water electrolysis

Subir Paul,[1-2] An Hardy,[1-3] Koen Vandewal,[1-3] Mohammadhosein Safari[1-3*]

[1]Institute for Materials Research, UHasselt, Martelarenlaan 42, B-3500 Hasselt, Belgium

[2]Energyville, Thor Park 8320, B-3600 Genk, Belgium

[3]IMEC division IMOMEC, BE-3590, Belgium

[*]Corresponding author: momo.safari@uhasselt.be

Abstract

Proton exchange membrane water electrolysis (PEMWE) stands out as a promising technology for producing highly pure hydrogen at high voltage efficiency and a minimal impact on the environment. The manufacturing method of the catalyst layer still needs more fine-tuning to improve the performance and lifetime of PEMWE even with notable progress in materials development. In this work, we showcase the sensitivity of the polarization at RuO_2 anode to the spatial distribution of the ionomer within the catalyst layer over short- and long-term operation. A series of anode electrodes with different formulations are systematically prepared and characterized to quantify the interplay between the components' spatial distribution and the polarization behavior during water electrolysis. The results point to the more efficient utilization of the catalyst particles in a graded electrode, substantiated by Tafel and voltammetry analysis. Electrochemical impedance spectroscopy identifies electronic and ionic charge transport as the dominating loss phenomena in the bulk and at interfaces, respectively. Our results suggest that the aging rate at the catalyst layer is influenced by the ionomer content and is higher close to the membrane. By exploring the formulation parameters of the graded catalyst layer, this work seeks to contribute to the development of more efficient PEM electrolysis systems, paving the way for a sustainable hydrogen economy.

1. Introduction

The pursuit of efficient and sustainable hydrogen production has intensified in recent years, driven by the urgent need to transition to cleaner energy sources. Proton-exchange-membrane water electrolysis (PEMWE) is a promising technology for the production of green hydrogen and a key component in the transition to a low-carbon economy.[1] PEMWE offers many advantages compared to the alkaline electrolyzers with respect to the hydrogen purity (99.999 vol%), compactness, response time, working pressure, and efficiency.[1-4] The progress of PEM electrolysis depends mostly on the development of very efficient catalyst layers, which are essential for the electrochemical reactions engaged. But PEM electrolysis's high capital cost, mostly related to the use of precious metal catalysts and the complicated structure of the membrane electrode assembly (MEA), limits its general acceptance.[5-7] The MEA includes a series of key components, namely the porous transport layer (PTL), the anode and cathode catalyst layers, and the membrane, each with a significant impact on the electrolysis performance (Figure 1a).

The anode catalyst layer stands out as a particularly vulnerable component in the PEMWE due to its exposure to highly oxidative and corrosive conditions and its relatively larger polarization compared to the cathode. The sluggish kinetics of the oxygen evolution reaction (OER) necessitate a higher loading of the iridium or ruthenium oxide (2-3 mg.cm^{-2} Ir/Ru) in the conventional anodes which is a hinderance to the feasibility of the large-scale industrialization of the PEMWE.[8-13] In this regard, there is an ongoing quest to discover alternative catalyst chemistries[14-18] on one hand, and to decrease the loading of the precious-metal particles in the catalyst layer through electrode engineering on the other hand.[19-23] One promising approach to enhancing the microstructure of the catalyst layer (CL), thereby improving mass and charge transport as well as the electrochemical kinetics of the OER, is to engineer the microstructure. For instance, unlike conventional CLs, it has been shown that a gradient in the distribution of the catalyst loading, ionomer content, and porosity can be advantageous to the mass transport and catalyst utilization and ultimately boost the overall performance of the PEMWE.[24-27] The available literature suggests that the optimal cell performance might be achieved by (i) increasing porosity and pore size while reducing ionomer film thickness (or ionomer loading) near the PTLto facilitate the transport of reactants and products and (ii) increasing the ionomer loading near the membrane to enhance the proton transport.[20] For instance, H. Liu et al. showcased the benefits of ionomer distribution in enhancing the stability and efficiency of PEMWE with an IrO_2/TiO_2 catalyst and Aquivion ionomer.[20] S. Dong et al. presented a novel anode design with a gradient ordered structure and low iridium loading using an Anodic Aluminum Oxide (AAO) template, significantly enhancing the performance and stability of PEMWE.[19] H. Lv et al. showed how a synergistic non-uniform distribution of IrO_2, TiNX (where X represents a non-stoichiometric amount of nitrogen), and ionomer content effectively reduces the loss of internal voltage at the anode for PEM water electrolysis.[21]

Following recent reports on the benefits of a graded catalyst design, this paper aims to shed more light on the design principles for graded catalyst layers, focusing particularly on the case of RuO_2 as the anode catalyst in two distinct loading zones—low and high. To the best of our knowledge, this is the first systematic study on a graded RuO_2-based catalyst layer for the PEMWE. To put our contribution in perspective, a comparative summary of the related literature on the graded catalyst layer is listed in Table S1. The main distinguishing feature of our work is the employment of a series of non-intrusive electrochemical tests to quantify the polarization and loss phenomena in a graded electrode over short- and long-term electrolysis. It also conducts an in-depth electrochemical impedance spectroscopy (EIS) analysis to quantify key polarization sources within the catalyst layer, which has been less explored in the literature. To do so, the sensitivity of the cell polarization to the adjustable design parameters including the total loading of the RuO_2 catalyst and the spatial distribution of the ionomer in a bilayer CL will be showcased. A home-made PEMWE is used to conduct water electrolysis (Figure 1b) over short and long-term while a series of in-depth microstructural and electrochemical techniques are employed to quantify the different sources of polarization.

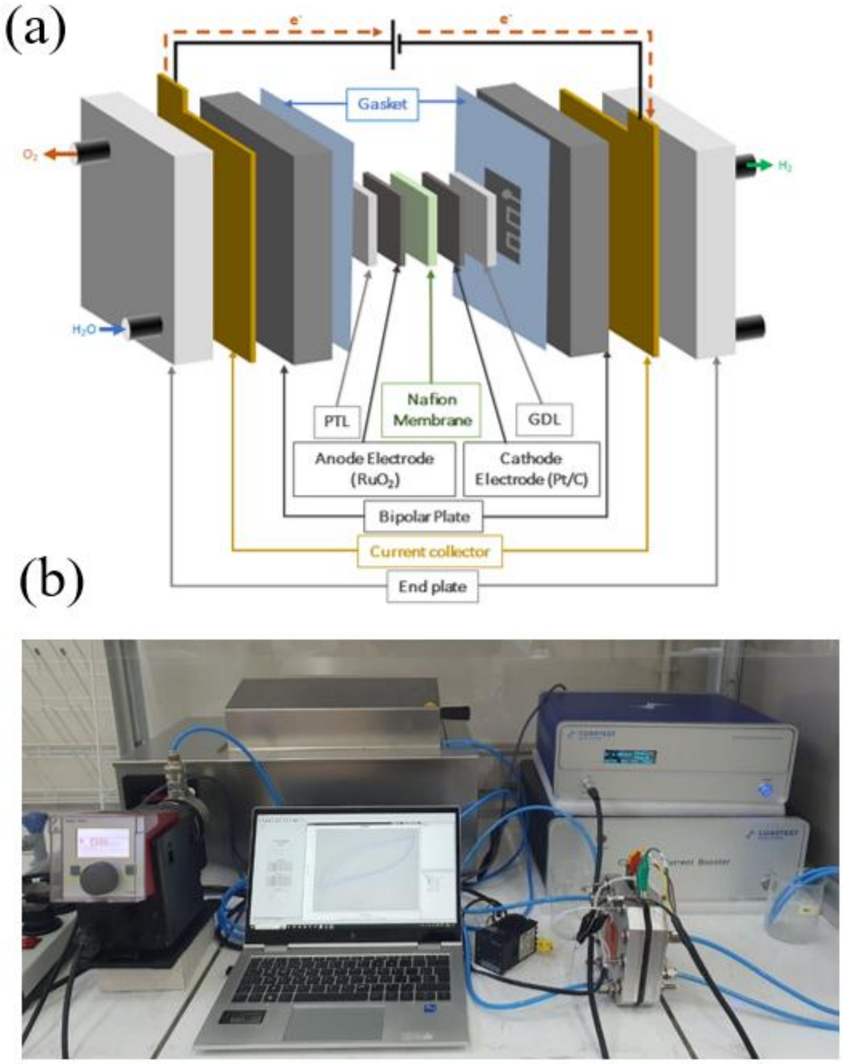

Figure 1. **(a)** Schematic view of a PEM water electrolyzer cell and its main components, **(b)** PEMWE experimental test bench used for the evaluation of the RuO_2 catalyst layers in this study.

2. Materials and Methods

2.1. Ink formulation, coating, and MEA fabrication

The inks for the anode catalyst were prepared in a multi-step process. A solution of 5 wt% Nafion (D520, 5% ionomer from Fuel cell store) was added to a mixture of 2-propanol (purity≥99.9% from Sigma Aldrich) and De-Ionized (DI) water (18 MΩcm). To ensure sufficient dispersion the mixture was sonicated for 15 minutes. Then, the RuO_2 (Sigma Aldrich, 99.9% trace metals basis) catalyst was added and mixed for 60 min in an ultrasonic bath from Fisherbrand Bath Sonicator operating at approximately 120 W and 37 KHz, with intermittent magnetic stirring for 2 minutes every 15 minutes to minimize agglomeration. The dispersion process was conducted at room temperature (~25 °C) without active cooling. All catalyst inks were formulated with 1.5 wt% total solids (comprising both catalyst and ionomer) and 98.5 wt% solvent, consisting of a mixture of 20 vol% 2-propanol and 80 vol% deionized water. The loadings for the catalyst and ionomer within the slurries are found based on the target anode composition in the experimental design set (Table 1, and Figure. 2).

Prior to ink deposition, the ultra-thin titanium porous transport layer (Grade 2 titanium; thickness: 0.010 inches [~250 µm]; without corrosion protection; average pore size: 5–10 µm; porosity: ~30%, from Fuel Cell Store) was dried in an oven at 80 °C and weighed using a Sartorius analytical balance with ±0.001 mg accuracy to determine the initial weight. The prepared ink was then deposited onto the PTL using an airbrush coating technique for precise control. A Fengda FE-182 double-action airbrush equipped with a 0.5 mm nozzle was employed for catalyst layer deposition. The Fengda FD-182 Airbrush mini compressor was set to a pressure of 2 kg/cm^2 to ensure optimal ink atomization.

A single coating pass was sufficient for the ungraded catalyst layers, but for graded catalyst layer electrode two different ink with specific ionomer content was prepared and deposited one after another. The sample was dried for 6 minutes at 80 °C after each coating in order to evaporate the solvent. Until the desired catalyst's loading was reached, this process was repeated. The final weight of the PTL with the catalyst layer was measured again to determine the final catalyst loading at anode, targeting a value of 2 ± 0.1 mg cm^{-2} for samples in group #1 (sample # 1-3) and 1 ± 0.1 mg cm^{-2} for samples in group #2 (samples # 4-6). The airbrush was thoroughly cleaned with isopropanol (IPA) before and after use to prevent contamination.

The MEA was prepared by stacking the cathode (purchased from fuel-cell store) containing 0.5 mg/cm^2 60% platinum on Vulcan - carbon cloth electrode, the Nafion 117 membrane (from fuel-cell store), and the anode catalyst-coated PTL, using a hot press (P 200S Colin) for 3 minutes at 155 °C and 25 bar to ensure an optimal contact between the different layers.

Table 1. Composition of the various cathode catalyst layers (CCL) prepared in this study.

		Layer 1 (Near PTL)			Layer 2 (Near membrane)			Total loading	Total ionomer
		RuO_2 Loading	ionomer content	ionomer weight	RuO_2 Loading	ionomer content	ionomer weight		
		(a)	(b)	(c)	(d)	(e)	(f)	a+d	c+f
		(mg/cm^2)	(wt%)	(mg/cm^2)	(mg/cm^2)	(wt%)	(mg/cm^2)	(mg/cm^2)	(mg/cm^2)
Group 1	Sample 1	2.0	15	0.353				2.0	0.35
	Sample 2	1.0	10	0.111	1.0	20	0.250	2.0	0.36
	Sample 3	1.0	20	0.250	1.0	10	0.111	2.0	0.36
Group 2	Sample 4	1.0	15	0.176				1.0	0.18
	Sample 5	0.5	10	0.056	0.5	20	0.125	1.0	0.18
	Sample 6	0.5	20	0.125	0.5	10	0.056	1.0	0.18

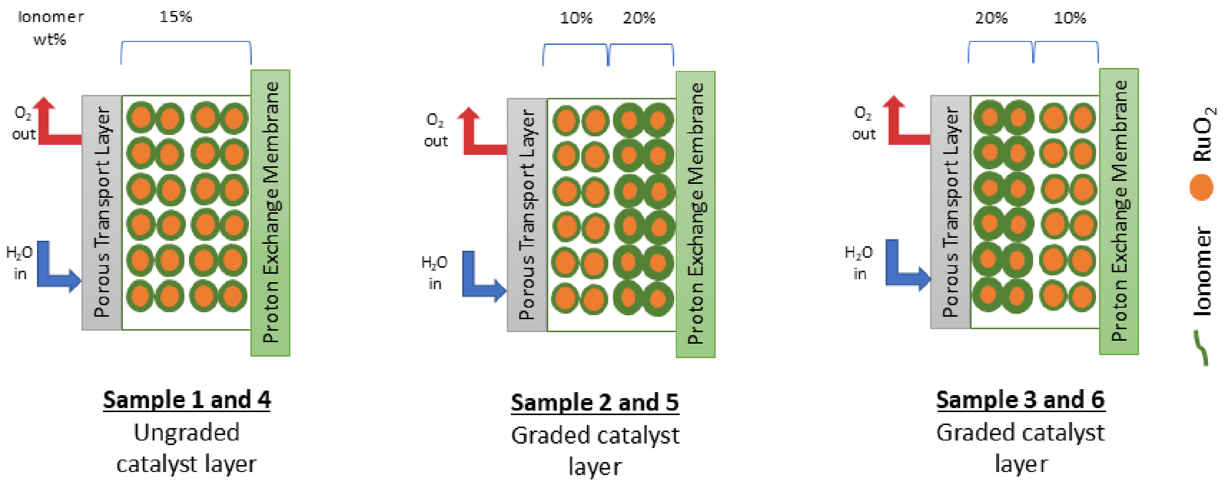

Sample 1 and 4
Ungraded catalyst layer

Sample 2 and 5
Graded catalyst layer

Sample 3 and 6
Graded catalyst layer

Figure 2. A schematic illustration of a bilayer anode catalyst layer with a non-uniform distribution of ionomer between the PTL and membrane.

2.2. Porosity measurement

The porosity and pore size distribution of the catalyst layer coating on the porous transport layer (PTL) were measured using a mercury porosimeter (Micromeritics, AutoPore IV 9600). This method was used with an applied pressure from 0 to 30,000 psi in equilibration mode. The system was allowed to equilibrate at each pressure before stepping to the next pressure for 10 seconds. It is based on the principles of capillary pressure determining how much liquid can penetrate a microporous system. Porosity (ε) was calculated based on the cumulative pore volume of the catalyst layer, i.e. $\varepsilon = \frac{Vpore}{Vbulk} \times 100$, where V_{bulk} and V_{pore} are the bulk volume and pore volume of the catalyst layer, respectively.

2.3. Electrochemical characterization

An in-house test bench was used to evaluate the impact of ionomer gradients on RuO_2 anode performance (Fig. 1a,b). The system included a 5 cm^2 electrolyser cell from Fuel Cell Store with a pin flow field design, a water heater bath, a water pump, and a potentiostat and booster. The cell was assembled using eight M8 screws, each tightened to a torque of 40 in-lb. Reinforced gaskets were used to resist dimensional instability and lateral extrusion. Deionized water (2 mL min^{-1} cm^{-2}) was heated to 80 °C by passing through a thermal bath (from MEMMERT WTB11) and supplied to the anode compartment of the cell using a precision pump (Fink Chem R033). A temperature controller from Inkbird and a heater pad attached to the cell maintained constant cell temperature throughout the tests. Commercial systems inherently function at significantly elevated pressures (10–30 bar), may utilize reinforced membranes and/or porous transport layers designed for industrial durability, and possess substantially greater active surfaces (≥100 cm^2). Nonetheless, our design maintains essential transport and electrochemical characteristics, and the performance trends noted—especially with catalyst layer design—are anticipated to extend to larger systems, although additional scale-up investigations are required.

Before experiments, the cell was conditioned according to a protocol consisting of a sequence of galvanostatic and potentiostatic steps for 80 °C: 1 hour of 0.2 A/cm², 1 A/cm² for a further hour, and holding at 1.7 V until current stabilized (variation of less than 5%).

The polarization curves were measured in the current-controlled mode (galvanostatic) within a range of 0 to 2.0 A/cm^2 using a potentiostat (Corrtest Potentiostat/Galvanostat model CS310 and 20 A Current booster CS2020B). The current was sequentially increased in step sizes of 20, 40, and 100 mA/cm^2 for the (0 A/cm^2 - 0.2 A/cm^2), (0.2 A/cm^2 – 0.4 A/cm^2), and (0.4 A/cm^2 - 2.0 A/cm^2) ranges, respectively. The cell was held at each current level for 5 min of which the average of voltage readings during the last 1 min were registered as the steady state voltage corresponding to each current and used to plot the polarization curves. The stability was evaluated under a constant current density of 1 A/cm² over a duration of 100 hours at 80 °C. Potentiostatic electrochemical impedance spectroscopy (EIS) was performed with different cell voltage backgrounds (1.3 to 1.7 V) while superimposing a sinusoidal perturbation with a 10 mV amplitude at different frequencies, from 300 KHz to 0.1 Hz.

Two polarization curves and EIS were measured per sample, one immediately after the conditioning process, termed 'initial', and the second after a 100 hour durability test for a given sample, termed 'final'. The electrochemical active surface area of the several RuO_2 samples were measured using cyclic voltammetry (CV) with several RuO_2 sample as the working electrode in the same electrolysis cell and using a water flowing rate of 5 ml min-1 at 80 °C. The working electrode potential was swept from 0.1 to 1.3 V at a scan rate of 50 mV s^{-1} with respect to a pseudo-hydrogen-reference electrode (p-HRE). As a dual-purpose cathode and reference, the p-HRE used the same platinum formulation as employed for the electrolysis tests; the only difference was that it was purged with dry hydrogen at 50 ml min-1 during the CV tests. To ensure reproducibility, cyclic voltammetry measurements were repeated 10 times per MEA, and the experiment was conducted on three identically fabricated MEAs.

3. Results and Discussion

3.1. Physical characterization

Mercury intrusion porosimetry (MIP) analyses were conducted to examine the influence of MEAs formulation details on the pore size distribution and porosity of the catalyst-coated PTL (Figure 3). The pores in the 5-20 µm range belong to the PTL (red line). However, in the lower range of 0.2 to 2 µm, only catalyst-coated samples show peaks, which assigns this range of pore sizes to the catalyst layer. The total porosity of the PTL sample is 26.56%, while the CL coated samples have a higher porosity in the range of 28.4% to 31.2%. The porosities of the samples #1 through #6 are 28.4% ± 2%, 28.46% ± 1%, 29.83% ± 1%, 31.26% ± 2%, 29.52% ± 1%, and 30.88% ± 1%, respectively. Noteworthy is the average higher porosity of the samples # 4-6 compared to samples # 1-3 suggesting that the overall impact of the lowering in the loading of catalyst and ionomer is a rise in the porosity of the catalyst layer. However, the porous volume in the range below and above 3 µm is higher and lower, respectively, in samples #1-3 compared to the samples #4-6. We speculate that this observation mainly reflects the potential dominant destructive impact of overloading in ionomer content on the pore formation in the catalyst layer, particle agglomeration, and pore clogging.[28] The differences between the samples in each category of high (1-3) and low (4-6) catalyst-loading are minor indicating that the overall porosity of the catalyst layer is not sensitive to the spatial distribution of the catalyst and ionomer in the samples with graded design, and is only a function of the total loading of the ionomer and catalyst.

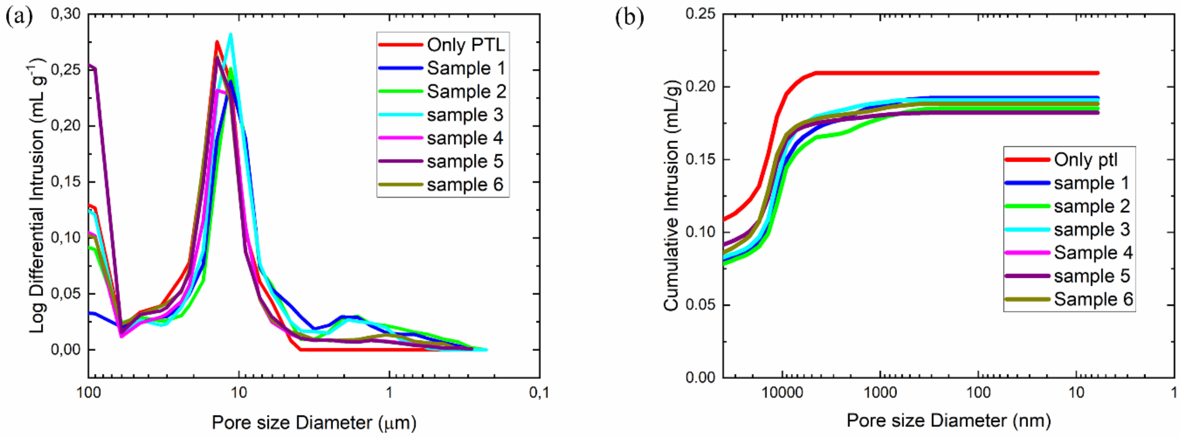

Figure 3. **(a)** Distribution of mercury volume across different pore sizes for the bare PTL and 6 catalyst-coated PTL Samples (Table 1). **(b)** Cumulative intrusion vs. pore size. The porosity values were calculated based on the total pore volume of the samples including the PTL and the catalyst layer. samples 1–3: RuO_2 loading: 2 mg/cm^2, ionomer loading: 0.36 mg/cm^2, samples 4–6: RuO_2 loading: 1 mg/cm^2, ionomer loading: 0.18 mg/cm^2.

3.2. Polarization and OER kinetics

Steady-state polarization curves at 80°C and ambient pressure are presented in Figure 4a and Figure 4b for samples # 1-3 and 4-6, respectively. It is noteworthy that some of the polarization curves exhibit a curvature which is not a common observation in the literature. We speculate that this feature stems from the temporal two-phase flow instabilities inside the electrodes and the flow channels.[29] In our setup, we work without an active backpressure arrangement which increases the chance for the accumulation of the gas bubbles and voltage fluctuations. The measurements were conducted both at the pristine state and after the durability test, i.e. 100-hour continuous electrolysis at 1 A/cm^2 (Figure 4c). At the pristine state, the overpotential ($\eta = E - E_0$) for water splitting lies in a similar range for the samples in group # 1 and # 2 and lies between 0.11 to 0.82 V (Figure 4 d-e) assuming an equilibrium voltage of $E_0 = 1.18$ V at 80°C.[30] The highest polarization is observed for graded samples with higher loading of ionomer at PTL/catalyst-layer interface, samples 3 and 6. The overpotential reaches 0.82 V for sample 3 and 6 at a current density of 1.7 A/cm^2 and 1.5 A/cm^2, respectively. However, at the same overpotential, the samples rich in ionomer at membrane/catalyst-layer interface can sustain electrolysis at a higher current density. At 0.82 V, samples 2 and 5 reach a current density of 2 and 1.8

A/cm^2, respectively. At currents above 1 A/cm^2, sample 2 enables water electrolysis with a 50 – 70 mV lower overpotential compared to sample 1. Samples 4 and 5 with a lower total RuO_2 loading in the catalyst layer demonstrate a similar polarization behavior to the samples 1. This means that at the pristine state, there is no added value in increasing the catalyst loading from 1 to 2 mg/cm^2 in the absence of an optimal distribution of ionomer within the catalyst layer.

During the durability test, all samples experience a gradual increase of the electrolysis voltage at 1 A/cm^2 (Figure 4c). Samples in group # 2, with a lower total loading of the ionomer show a lower rate of voltage increase, hereafter referred as *dynamic aging*. Samples in group 2 have a dynamic aging of 0.77 mV/hr compared to that of the samples in the first group (0.93 mV/hr). Samples with more ionomer near the membrane (2 & 5) demonstrate a lower dynamic aging compared to those enriched with the ionomer near the PTL (3 & 6). These observations suggest that the ionomer loading and its spatial distribution within the catalyst layer have a non-negligible impact on the aging behavior of the cell. A comprehensive postmortem aging analysis is essential to determine the aging mechanisms which is beyond the scope of this paper. However, we speculate that a combination of the corrosion at the PTL/catalyst interface, degradation of the ionomer, and catalyst agglomeration and detachment can explain the aging behavior of our cells.[31-32] Particularly, the corrosion of a bare unprotected Ti-based PTL has been shown to have a cascading effect, triggering further degradation at the catalyst layer.[31] In this regard, our data suggest that a higher concentration of the ionomer near the PTL/catalyst layer interface can accelerate the corrosion rate of an unprotected PTL. This speculation is further corroborated by the EIS investigations in section 3.3 where the contact resistance within the cell is shown to increase faster at higher concentrations of the ionomer in the catalyst layer. A complementary insight about the aging can be obtained from the static polarization behaviors at the end of the durability tests (Figure 4 a-b). The lowest and highest static polarization after 100 hours of continuous operation belongs to the sample 2 (η=60 mV at 1 A/cm^2) and 6 (η=70 mV at 1 A/cm^2), respectively. It is noteworthy that sample 2 is the only sample to sustain a current above 1.5 A/cm^2 with an electrolysis voltage below 2V after the durability test. Moreover, the relative increase of static polarization between the pristine and final aged state is on average lower for the samples in the second group (77 mV) compared to that of the first group (90 mV). This is in line with the conclusion drawn from the dynamic aging analysis with regard to the important role of ionomer content and spatial distribution in the degradation of the samples. Another point of attention is the mismatch between the cell polarization after the 100-hour durability test, calculated based on the dynamic voltage (Figure 4c) and static polarization data (Figure 4 a-b). After the durability test, we observe a voltage mismatch ranging from -10 to +20 mV between the static and dynamic voltage at 1 A/cm^2 (Table S2). This suggests that the long-term continuous electrolysis, which is a common practice to evaluate the aging rate of an electrolyzer, might underestimate or overestimate the static polarization behavior of the cell. This observation highlights and corroborates the earlier reports on the influence of the operation mode and cycling protocol on the aging dynamics of the PEMWE.[33] We speculate that the variation of polarization mismatch between the static and dynamic voltages within our samples should be interpreted in the context of different extents of reversible and irreversible degradation of the samples. The accelerated aging and durability tests with dynamic load profiles are particularly important for the connection of PEMWE with intermittent power input from renewable sources such as wind and solar.[34] The limited literature on the accelerated aging tests with dynamic load profiles suggest that the cyclic variation of the current density has significant impact on the aging and degradation of the PEMWE with both positive[34] and negative impact[35] on the durability. Particularly, the open-circuit or shutdown periods within a load profile can trigger specific types of degradation mechanisms such as the change in the oxidation state of the catalyst centers at the anode following the H_2 crossover to the anode compartment.[36] This phenomenon can partly explain the voltage recovery or reversible degradation after dynamic aging tests. The *current reversal* is another complication concerning the open-circuit periods where the residual H_2 and O_2 gases at the cathode and anode, respectively, can temporarily transform the PEMWE to a fuel cell.[37] Under such a circumstance, the Pt dissolution and its migration to and deposition at the membrane has been reported in the literature.[36] Further research is required to investigate the mechanistic details behind the mismatch between the static and dynamic voltages after our durability tests. Moreover, considering the lifetime target for commercial PEMWEs (> 50.000 hours) longer durability tests are essential to assess the aging behavior of our samples under realistic load profiles.[38]

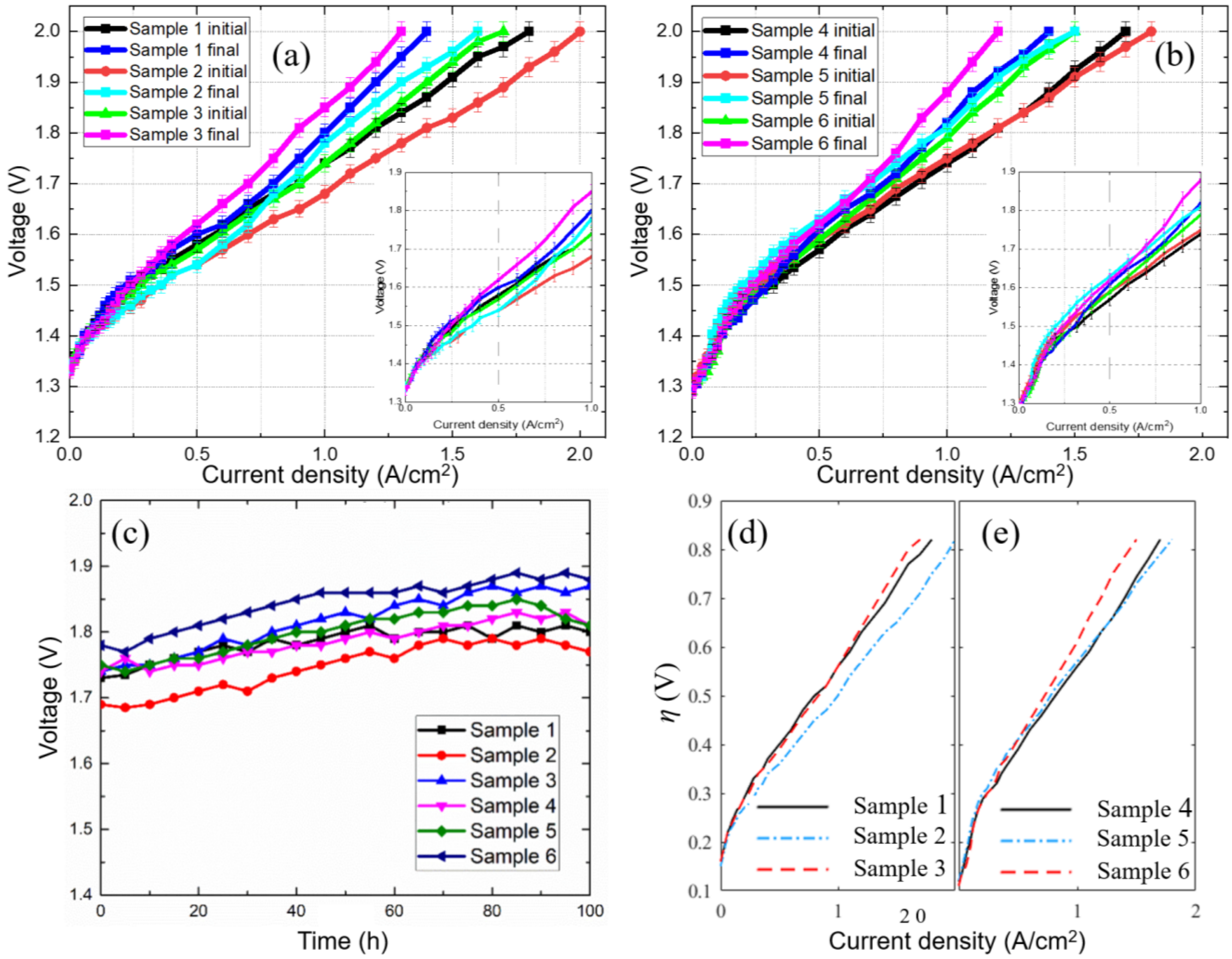

Figure 4. Ambient pressure polarization curves at 80°C for the 5 cm² single-cell PEM-WE, measured for the pristine samples (initial) and after 100-hour durability test (final) for two sample groups with different RuO_2 and ionomer loadings: **(a)** samples 1–3 (catalyst: 2 mg/cm^2, ionomer: 0.36 mg/cm^2), **(b)** samples 4–6 (catalyst: 1 mg/cm^2, ionomer: 0.18 mg/cm^2). **(c)** cell voltage evolution during the 100 hours durability test at

1 A/cm^2. **(d-e)** the electrolysis overpotential (η) as a function of the current density at the pristine state based on the static polarization date in (a-b). Figure insets (a)-(b) magnify the polarization plots in the current window 0-1 A/cm^2.

The polarization data from Figure 4a-b were corrected for the ohmic losses (see supporting information) and plotted with a logarithmic current coordinate (Figure 5 a-b). This data representation enables the calculation of the Tafel slopes after a linear fit of the data within the 10–100 mA/cm^2 range, where voltage losses are mainly caused by kinetic limitations while charge and mass transport limitations are negligible.[39] As such, considering the very high exchange current density of the HER relative to the OER, the comparison of the Tafel slopes among the samples reflects the difference in their OER kinetics at the anode.[40] The average Tafel slope reads 61 mV/dec for samples in group #1 compared to 71 mV/dec for samples in group #2. This apparent faster kinetics for group 1 is expected since the catalyst loading is higher which offers a higher electrochemically active surface area (ESA) for the oxygen evolution. It is needless to mention that the Tafel slope is representative of the intrinsic kinetics of a redox reaction and expected to be independent of the ESA. However, the sensitivity of the Tafel slope to ESA is not surprising when the electrode cross-section is used to normalize the current, instead of ESA, and the Tafel analysis is performed within a fixed current window, e.g. 0-100 mA/cm^2. This means that the variation of the Tafel slope in our samples correlates with the variations in the electrochemically active surface area of the electrodes. In this regard, the intra-group variations of the Tafel slopes at the pristine and aged state hints at the impact of the catalyst-layer formulation on the ESA. For instance, at the pristine state, sample #4 shows a Tafel slope which is 4% and 22% higher than those of sample #5 and #6, respectively, although they contain the same loading of catalyst. This observation suggests that the non-uniform distribution of the ionomer between the PTL and membrane is in favor of exposing a higher fraction of the catalyst loading to the OER compared to the conventional single-layer coated catalyst layers. In other words, the over-shielding of the catalyst particles with the ionomer can be avoided with a gradient design for the catalyst layer.

The double-layer capacitance (C_{dl}) and the non-faradic voltammetry charge (q) are often used as the indirect and relative measures of the ESA for the oxide-based OER catalysts.[41-42] We recorded the cyclic voltammograms (CV) of the pristine samples #1-6 within 0.1 to 1.3 V vs. RHE using a scan rate of 50 mVs^{-1} (Figure 5c) to estimate the C_{dl} and q. The C_{dl} was approximated based on the average current associated with the (dis)charge of the double layer (Δj / 2, Figure 5c) and the scan rate (ν), i.e. $C_{\mathrm{dl}} = \frac{(\Delta j/2)}{\nu}$, and q was obtained by the integration of the cyclic voltammogram within 0.1 to 1.3 V vs. RHE voltage window (Table S3). The double-layer capacitance measurements were repeated with three identical MEAs and found to be uniform with a variation below 7%. The samples with higher C_{dl} and q are those with the lower Tafel slope (Figure 5d, Figure S1) and this observation substantiates the presence of a direct link between the ESA, C_{dl} and q. These results suggest that the graded design of the catalyst layer enables a more effective utilization of the catalyst loading and therefore proves to be a viable option for decreasing the loading of the precious catalyst materials in the catalyst layer.

The impact of long-term electrolysis on the Tafel slope varies among the samples. The Tafel slope decreases by 5%, 12% for samples #2 and #4, respectively at the end of durability tests. Samples #5 demonstrates insignificant change in the Tafel slope while that of sample #3, #1, and #6 increase by 7%, 8%, and 17%, respectively. We speculate that the apparent increase of ESA leading to the decrease in Tafel slope might be a consequence of an increased roughness of the catalyst particles which is an early stage manifestation of the catalyst dissolution and degradation, but requires further dedicated post-mortem research for confirmation.[43]

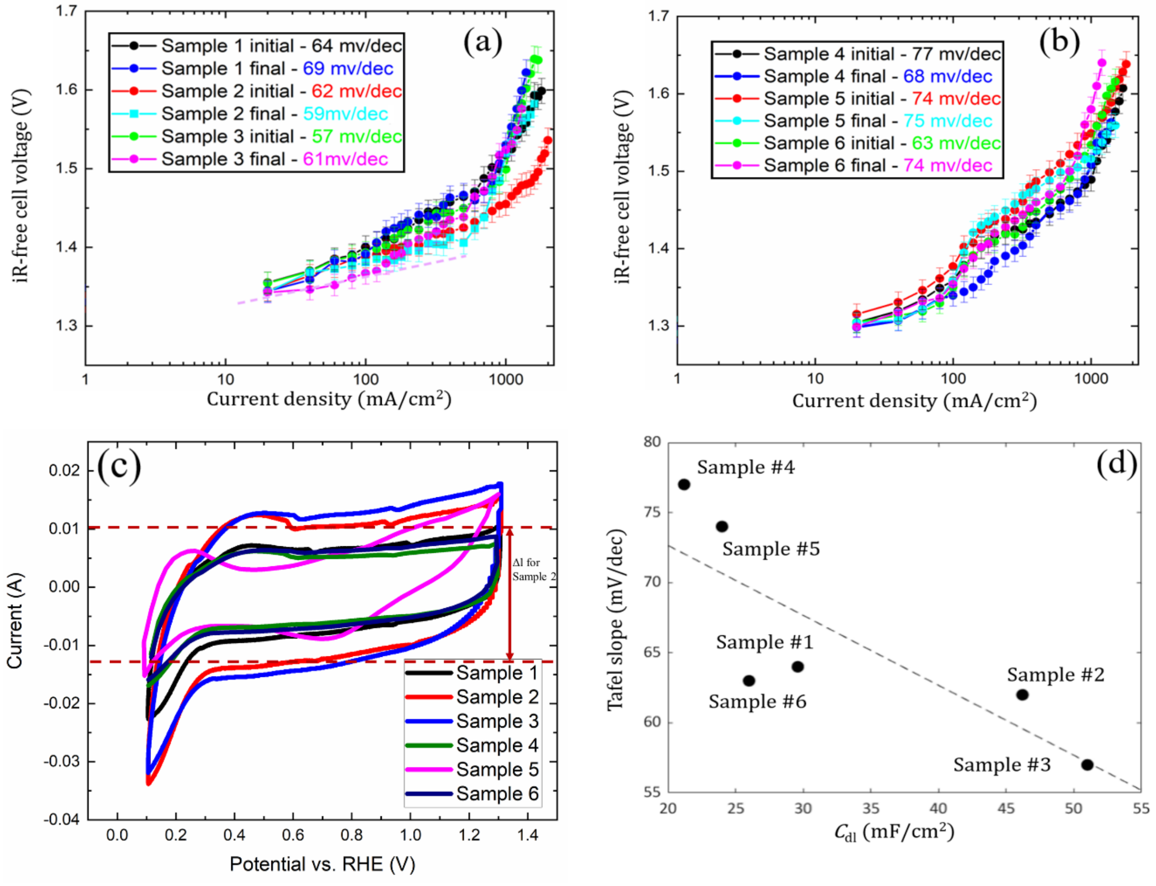

Figure 5. Tafel plots based on the polarization data corrected for ohmic drop for two sample groups with different RuO_2 and ionomer loadings: **(a)** samples 1–3 (catalyst: 2 mg/cm^2, ionomer: 0.36 mg/cm^2), and **(b)** samples 4–6 (catalyst: 1 mg/cm^2, ionomer: 0.18 mg/cm^2). The Tafel slopes were obtained based on a linear fit to the data within the current range 10–100 mA/cm^2. **(c)** cyclic voltammograms of samples #1-6 at the pristine state recorded at 50 mv/s **(d)** the correlation between the Tafel slope and the double-layer capacitance (C_{dl}) of the samples #1-6 at the pristine state.

3.3. Electrochemical impedance spectroscopy

Electrochemical impedance spectroscopy (EIS) is one of the widely used technique for identifying different ohmic and non-ohmic contributions to the overall impedance of an electrochemical systems including PEMWE.[44] The EIS spectra were recorded for the six samples at open-circuit (OCV) and various background voltages (1.3 to 1.7 V) for two different states of the cells, i.e. pristine and after 100 hr of continuous electrolysis at 1A/cm^2 (Figure 6a-b and Figure S2-3). The experimental EIS data were analyzed with an electrical equivalent-circuit model using Zview software to quantify the different sources of polarization in the cells. The circuit consists of one resistor in series with two R/CPE branches (Figure 6c).[8] The R_1 corresponds to the very high-frequency intercept on the real axis in the Nyquist plot and models the ohmic resistance of the cell induced by the limitations in the electrical and ionic conduction within the bulk components of the PEMWE. In the pristine state, the $R1$ is almost 80% higher in the samples of group #1 (77 mΩcm^2) relative to the second group (41 mΩcm^2) (Figure 6d, Figure S4). In this regard, the higher content of the ionomer in the group 1 implies that the bulk electronic conduction is more limited compared to the through-plane ionic conduction in our anode electrodes. The most and least bulk-resistive samples are sample #2 (90 mΩcm^2) and sample #6 (30 mΩcm^2), respectively (Figure S4). This observation suggests that the ionomer enrichment of the regions near to the membrane is the most destructive configuration for the overall bulk electronic conductivity of the catalyst layer. Under such circumstances, the accumulation of the ionomer next to membrane can hinder the electronic percolation between the PTL and the catalyst particles located closer to the membrane. In the aged state, both groups of samples experience on average an ~18% increase in bulk resistance. The highest rate of degradation in $R1$ belongs to sample #6 (Figure S4). This suggests that the ionomer-poor region next to the membrane is very vulnerable to the degradation.

The two R/CPE (resistor/constant-phase-element) elements account for the two arcs appearing at higher and lower frequencies. The interpretation of the first arc at higher frequencies is debated in the literature. Two major groups of explanations are noteworthy. In the first category, the high frequency semi-circle is ascribed to the hydrogen evolution reaction (HER)[8,45-47] or other charge transfer processes linked with the electrical and/or ionic conductive materials and oxides present in the catalyst layer.[8,48-50] The second category considers the interfacial contact resistances within the electrodes to cause the high-frequency arc.[51] We speculate that a combination of the two schools of thoughts is best representative of our samples. Particularly, we observe that the high-frequency arc is present even at OCV and before preconditioning of the cells which calls for the extra sources beside the HER and OER, namely the contact resistances between different layers in the MEA (Figure 6a-b, Figures S2-3). Moreover, the slight sensitivity of the diameter of this arc, quantified by R_2, to the background voltage suggests a minor role for the HER and possibly other activated redox reactions in our samples, e.g. some impurity metals or oxides within the catalyst sample. Moreover, the PTL used in this study is without a corrosion protective layer which makes it vulnerable to the corrosion and growth of passivation films on the surface of the PTL.[31] As such, we expect that the high-frequency arc in the Nyquist plot and the contact resistance R2 are partially contributed by the native oxide films on the Ti PTL layer and its further growth and evolution during the long-term operation. Moreover, the interactions between the ionic groups of the membrane and water result in a capacitive behavior at higher frequencies which contribute to the high frequency arc in the EIS spectra.[52] In the pristine state, the two groups of samples on average share a very similar range of contact resistance ($R2$), i.e. 160 mΩcm^2 for group #1 vs. 200 mΩcm^2 for group #2 (Figure S5). Sample #6 and sample #2 have the highest and lowest contact resistance which suggests that the ionic contact-resistance is more limiting compared to the electronic contact in the pristine samples. The average rate of increase in the contact resistance is higher (32%) for group #1 compared to the group #2 (20%). Considering the higher content of ionomer in group #1, it is legitimate to assume a strong link between the ionomer concentration and the interfacial side reactions such as PTL corrosion and degradation of the ionic contacts within the cell which manifest in the rise of $R2$. The most unstable sample with respect to the contact resistance is sample #3 with 54% rise in $R2$ after stability tests. The lowest rate of change in $R2$ after durability test is observed for sample #6 (7%). This sample has the lowest loading of ionomer next to the membrane while sample #3 has the highest loading of ionomer next to the PTL. As such, we speculate that a PTL-catalyst-layer interface rich in ionomer (~ 0.250 mg/cm^2) has a relatively poor long-term stability.

The arc at lower frequencies (<1kHz) corresponds to the charge-transfer resistance of the more sluggish oxygen evolution reaction (OER).[51] For all six samples, both in their pristine state (initial) and after stability test (final), the diameter of the low-frequency arc, quantified by R_3, decreases with increasing the background voltage (Figure 6f, Figure S6) which shows the kinetics enhancement for the oxygen evolution reaction at higher overpotentials (OER).[53] In the pristine state, the charge-transfer resistance of the samples in the group #2 (2198 mΩcm^2) is on average significantly higher than that in the group #1 (448 mΩcm^2). The R_3 reads the lowest and highest for sample #3 (213 mΩcm^2) and #5 (3792 mΩcm^2), respectively. The charge-transfer resistance is inversely correlated with the ESA within the catalyst layer being the effective area of the triple points which ionically and electronically are wired to the PTL and membrane while in contact with the reactant, i.e. water. Therefore, the very high $R3$ of sample 5, with a very ionomer-rich catalyst layer next to the membrane, suggests that a fraction of catalyst particles is over-shielded because of excessive ionomer loading and are therefore disconnected from the electronic percolation network of the anode (Figure S6). Moreover, the ionomer-poor region next to the PTL might suffer from an insufficient coverage of the catalyst particles rendering a part of the layer inactive for the OER. The same line of reasoning can be used to explain the very low $R3$ of sample 3. In this sample, the distribution of the ionomer between the PTL (0.235 mg/cm^2) and membrane (0.118 mg/cm^2) sides of the catalyst layer seems optimal to ensure a sufficient ionic connectivity of the catalyst particles next to the PTL without being too much near the membrane to hinder the flow of electrons. The variation trend of the charge-transfer resistance among the samples parallels that of the Tafel slope, C_{dl} and q indexes highlighting the central role of the ESA in the kinetics behavior of the electrolysis cell (Figure S7). These indexes all point at samples #2 and #3 for the optimal utilization of the catalyst and identify sample #5 and #6 as the worst. Considering both aspects of initial activity and stability of the catalyst layer, sample 2 stands out as the best formulation. Sample #3 stands out with respect to the charge-transfer kinetics ($R3$, Tafel slope), ESA, and C_{dl}. At lower current densities, where the charge and mass transport limitations are negligible, the overall polarization behavior of the electrode is dictated by the charge-transfer kinetics. This explains the very competitive polarization behavior of sample #3 below 0.75 A/cm^2 (Figure 4a). However, the performance of this sample deteriorates sharply at higher current densities and after stability tests (Figure 4a, Figure 4c). This suggests that the spatial distribution of the ionomer in sample #3 promotes the catalytic activity of the electrode at its pristine state but hinders the charge and mass transport which are crucial to the polarization for electrolysis at higher current densities.

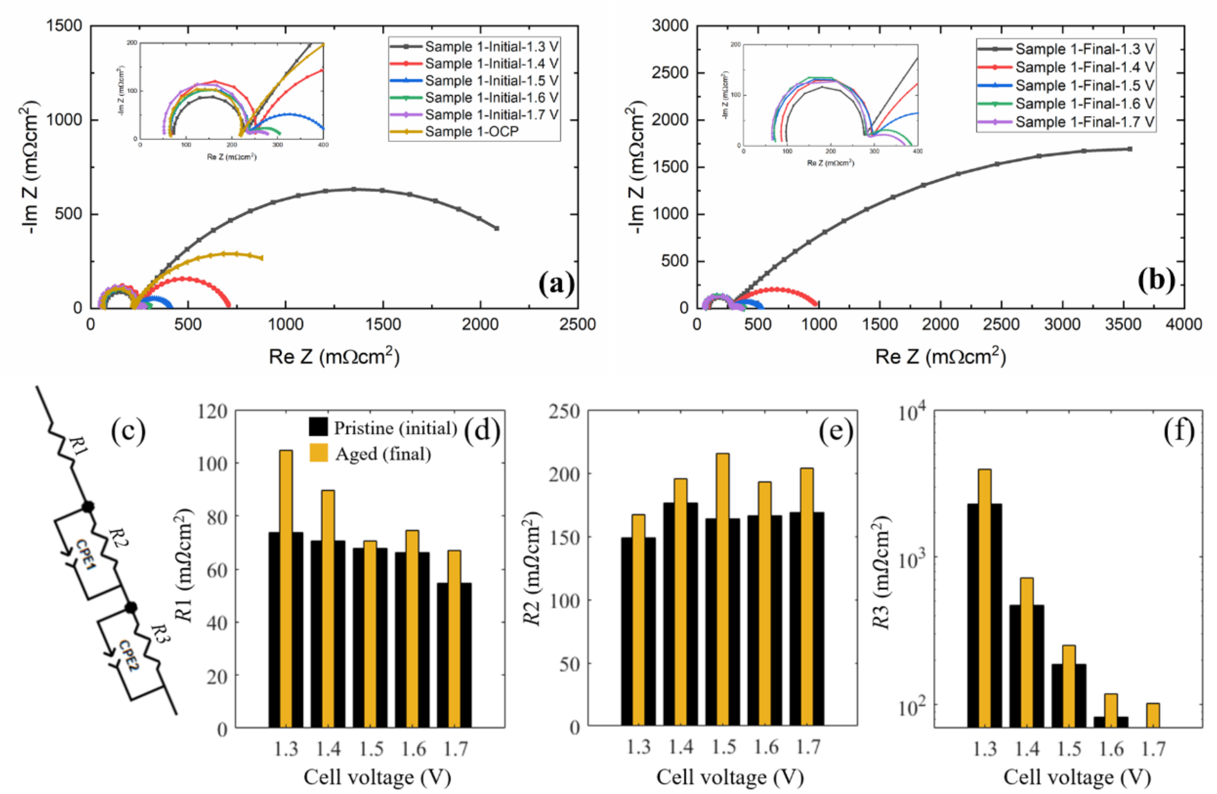

Figure 6: The Nyquist EIS plots of the sample #1 recorded within the frequency range 0.1 Hz–300 kHz and at different background voltages at **(a)** pristine, and **(b)** aged states. **(c)** Equivalent circuit for simulating the EIS spectra of the samples. The sensitivity of the circuit parameters to the background voltage and state-of-the-health of the sample #1 **(d)** *R*1: bulk ohmic resistance, **(e)** *R*2: contact resistance, **(f)** *R*3: charge-transfer resistance.

4. Conclusions

In this paper, we systematically investigated the impact of ionomer content and its spatial distribution on the short- and long-term performance of a RuO_2 catalyst layer for PEMWE. The OER kinetics and the polarization behavior of a series of graded catalyst layers were analyzed with the help of chronopotentiometry, voltammetry, and electrochemical impedance spectroscopy. The results suggest that the non-uniform distribution of ionomer between the PTL and membrane is a viable method to increase the effective electrochemically active surface area of the catalyst layer. Particularly, a similar polarization to a traditional uniformly coated catalyst layer was showcased to be reached with a graded coating but with a lower loading of catalyst. EIS analysis enabled the quantification of the major polarization sources within the catalyst layer. It was shown that the bulk electronic conduction is more limiting relative to the ionic conduction in the bulk of the catalyst layer. The contact resistance, however, was shown to be dominated by the ionic contacts compared to the electronic contacts. The short-term accelerated aging tests revealed that the rate of performance decay is proportional to the ionomer content and more pronounced at the regions near the membrane. Particularly, ionomer degradation seems to significantly increase the contact resistance of the cell.

To reach an optimal spatial distribution of the ionomer in the catalyst layer one needs to consider the collective impact of the ionomer concentration on the charge-transfer kinetics, charge/mass transport over short and long range, and aging of the electrode. For instance, our results revealed that the ionomer overloading at regions close to the PTL is destructive to the long-term stability while constructive to the ionic percolation within the electrode. Similarly, an ionomer-rich catalyst-membrane interface was found to be destructive to the long-range electronic conduction within the electrode while being beneficial to set up a less resistive ionic contact between the catalyst layer and the PEM membrane. Our primary optimization of the catalyst layer suggests that an optimal short- and long-term performance can be obtained with the allocation of 10% ionomer to the region close to the PTL and 20% near the membrane. Although the electrochemical techniques showcased to provide valuable and quantitative information about the kinetics and charge transport limitations of our cell, we did not visualize the internal microstructure of the catalyst layer. This shortcoming can be solved in future studies by employing techniques such as FIB-SEM tomography as well as X-ray computed tomography and radiography.

Supporting information

Additional experimental details, methods, uncertainty analysis, benchmarking against the state-of-the-art graded electrodes, and characterization results, including internal resistance and polarization data, Tafel slope, and double layer capacitance.

Acknowledgement

The authors are grateful to the BOF at Hasselt University for the financial support of this work in the context of the CleanH2 project.

Author Contributions

S. P designed and conducted all the experimental investigations, performed the data analysis, and wrote the original draft of the paper. A. H and K. V contributed to the data analysis and validation of the results. M. S conceived and supervised the study. The final draft of the paper was reviewed and edited by all authors.

Notes

The authors declare no competing financial interest.

References

(1) Liu, R.-T.; Xu, Z.-L.; Li, F.-M.; Chen, F.-Y.; Yu, J.-Y.; Yan, Y.; Chen, Y.; Xia, B. Y. Recent Advances in Proton Exchange Membrane Water Electrolysis. *Chem Soc Rev* **2023,** 52, 5652-5683.

(2) Chatenet, M.; Pollet, B. G.; Dekel, D. R.; Dionigi, F.; Deseure, J.; Millet, P.; Braatz, R. D.; Bazant, M. Z.; Eikerling, M.; Staffell, I. Water Electrolysis: From Textbook Knowledge to the Latest Scientific Strategies and Industrial Developments. *Chem Soc Rev* **2022**, *51* (11), 4583–4762.

(3) Selamet, Ö. F.; Becerikli, F.; Mat, M. D.; Kaplan, Y. Development and Testing of a Highly Efficient Proton Exchange Membrane (PEM) Electrolyzer Stack. *Int J Hydrogen Energy* **2011**, *36* (17), 11480–11487. https://doi.org/10.1016/j.ijhydene.2011.01.129.

(4) Shin, H. S.; Oh, B. S. Water Transport According to Temperature and Current in PEM Water Electrolyzer. *Int J Hydrogen Energy* **2020**, *45* (1), 56–63. https://doi.org/10.1016/j.ijhydene.2019.10.209.

(5) Ouimet, R. J.; Glenn, J. R.; De Porcellinis, D.; Motz, A. R.; Carmo, M.; Ayers, K. E. The Role of Electrocatalysts in the

Development of Gigawatt-Scale PEM Electrolyzers. *ACS Catal* **2022**, *12* (10), 6159–6171.

(6) Wang, Q.; Cheng, Y.; Tao, H. B.; Liu, Y.; Ma, X.; Li, D.; Yang, H. Bin; Liu, B. Long-term Stability Challenges and Opportunities in Acidic Oxygen Evolution Electrocatalysis. *Angewandte Chemie* **2023**, *135* (11), e202216645.

(7) Clapp, M.; Zalitis, C. M.; Ryan, M. Perspectives on Current and Future Iridium Demand and Iridium Oxide Catalysts for PEM Water Electrolysis. *Catal Today* **2023**, *420*, 114140.

(8) Liu, H.; Tao, H. B.; Liu, B. Kinetic Insights of Proton Exchange Membrane Water Electrolyzer Obtained by Operando Characterization Methods. *J Phys Chem Lett* **2022**, *13* (28), 6520–6531.

(9) Lazaridis, T.; Stühmeier, B. M.; Gasteiger, H. A.; El-Sayed, H. A. Capabilities and Limitations of Rotating Disk Electrodes versus Membrane Electrode Assemblies in the Investigation of Electrocatalysts. *Nat Catal* **2022**, *5* (5), 363–373.

(10) Lettenmeier, P.; Kolb, S.; Sata, N.; Fallisch, A.; Zielke, L.; Thiele, S.; Gago, A. S.; Friedrich, K. A. Comprehensive Investigation of Novel Pore-Graded Gas Diffusion Layers for High-Performance and Cost-Effective Proton Exchange Membrane Electrolyzers. *Energy Environ Sci* **2017**, *10* (12), 2521–2533.

(11) Wang, P.; Jia, T.; Wang, B. A Critical Review: 1D/2D Nanostructured Self-Supported Electrodes for Electrochemical Water Splitting. *J Power Sources* **2020**, *474*, 228621.

(12) Bühler, M.; Hegge, F.; Holzapfel, P.; Bierling, M.; Suermann, M.; Vierrath, S.; Thiele, S. Optimization of Anodic Porous Transport Electrodes for Proton Exchange Membrane Water Electrolyzers. *J Mater Chem A Mater* **2019**, *7* (47), 26984–26995.

(13) Ma, L.; Sui, S.; Zhai, Y. Investigations on High Performance Proton Exchange Membrane Water Electrolyzer. *Int J Hydrogen Energy* **2009**, *34* (2), 678–684. https://doi.org/10.1016/j.ijhydene.2008.11.022.

(14) Zheng, Y.; Zhang, F.; Wang, G.; Lai, D.; Zou, L.; Cheng, Q.; Li, J.; Zou, Z.; Yang, H. CO Induced Phase-Segregation to Construct Robust and Efficient IrRux@ Ir Core-Shell Electrocatalyst towards Acidic Oxygen Evolution. *J Power Sources* **2022**, *528*, 231189.

(15) Liu, D.; Lv, Q.; Lu, S.; Fang, J.; Zhang, Y.; Wang, X.; Xue, Y.; Zhu, W.; Zhuang, Z. IrCuNi Deeply Concave Nanocubes as Highly Active Oxygen Evolution Reaction Electrocatalyst in Acid Electrolyte. *Nano Lett* **2021**, *21* (7), 2809–2816.

(16) Luo, F.; Hu, H.; Zhao, X.; Yang, Z.; Zhang, Q.; Xu, J.; Kaneko, T.; Yoshida, Y.; Zhu, C.; Cai, W. Robust and Stable Acidic Overall Water Splitting on Ir Single Atoms. *Nano Lett* **2020**, *20* (3), 2120–2128.

(17) Wang, P.; Cheng, Q.; Mao, C.; Su, W.; Yang, L.; Wang, G.; Zou, L.; Shi, Y.; Yan, C.; Zou, Z. Regulation of Oxygen Vacancy within Oxide Pyrochlores by F-Doping to Boost Oxygen-Evolution Activity. *J Power Sources* **2021**, *502*, 229903.

(18) Zhu, J.; Wei, M.; Meng, Q.; Chen, Z.; Fan, Y.; Hasan, S. W.; Zhang, X.; Lyu, D.; Tian, Z. Q.; Shen, P. K. Ultrathin-Shell IrCo Hollow Nanospheres as Highly Efficient Electrocatalysts towards the Oxygen Evolution Reaction in Acidic Media. *Nanoscale* **2020**, *12* (47), 24070–24078.

(19) Dong, S.; Zhang, C.; Yue, Z.; Zhang, F.; Zhao, H.; Cheng, Q.; Wang, G.; Xu, J.; Chen, C.; Zou, Z.; Dou, Z.; Yang, H. Overall Design of Anode with Gradient Ordered Structure with Low Iridium Loading for Proton Exchange Membrane Water Electrolysis. *Nano Lett* **2022**, *22* (23), 9434–9440. https://doi.org/10.1021/acs.nanolett.2c03461.

(20) Liu, H.; Wang, X.; Lao, K.; Wen, L.; Huang, M.; Liu, J.; Hu, T.; Hu, B.; Xie, S.; Li, S.; Fang, X.; Zheng, N.; Tao, H. B. Optimizing Ionomer Distribution in Anode Catalyst Layer for Stable Proton Exchange Membrane Water Electrolysis. *Advanced Materials* **2024**, *36* (28). https://doi.org/10.1002/adma.202402780.

(21) Lv, H.; Sun, Y.; Wang, S.; Chen, J.; Gao, Y.; Hu, D.; Yao, H.; Zhang, C. Synergistic Gradient Distribution of IrO2/TiNX Ratio and Ionomer Content Reduces the Internal Voltage Loss of the Anode Catalytic Layer in PEM Water Electrolysis. *Appl Energy* **2024**, *363*, 123012.

(22) Nguyen, H.; Sultanova, D.; Heizmann, P. A.; Vierrath, S.; Breitwieser, M. Improving the Efficiency of Fully Hydrocarbon-Based Proton-Exchange Membrane Fuel Cells by Ionomer Content Gradients in Cathode Catalyst Layers. *Mater Adv* **2022**, *3* (23), 8460–8468. https://doi.org/10.1039/d2ma00761d.

(23) Reshetenko, T.; Kulikovsky, A. Impedance Spectroscopy Study of the PEM Fuel Cell Cathode with Nonuniform Nafion Loading. *J Electrochem Soc* **2017**, *164* (11), E3016–E3021. https://doi.org/10.1149/2.0041711jes.

(24) Siracusano, S.; Pantò, F.; Tonella, S.; Oldani, C.; Aricò, A. S. Reinforced Short-Side-Chain Aquivion® Membrane for Proton Exchange Membrane Water Electrolysis. *Int J Hydrogen Energy* **2022**, *47* (35), 15557–15570.

(25) Sui, W.; Li, W.; Zhang, Z.; Wu, W.; Xu, Z.; Wang, Y. Efficient and Durable Electrochemical Oxygen Reduction to H2O2 in Acidic Media Assisted through Catalyst Layer Design. *J Power Sources* **2023**, *556*, 232438.

(26) Lv, H.; Wang, S.; Sun, Y.; Chen, J.; Zhou, W.; Zhang, C. Anode Catalyst Layer with Hierarchical Pore Size Distribution for Highly Efficient Proton Exchange Membrane Water Electrolysis. *J Power Sources* **2023**, *564*, 232878.

(27) Shahgaldi, S.; Ozden, A.; Li, X.; Hamdullahpur, F. Cathode Catalyst Layer Design with Gradients of Ionomer Distribution for Proton Exchange Membrane Fuel Cells. *Energy Convers Manag* **2018**, *171*, 1476–1486.

(28) Benedikt Karan. Influence of the Ionomer Content and Dispersion Solvent on the PEMWE Performance and Stability (Doctoral Dissertation, Technische Universität Wien)., 2021.

(29) Choi, Y.; Lee, W.; Na, Y. Effect of Gravity and Various Operating Conditions on Proton Exchange Membrane Water Electrolysis Cell Performance. *Membranes* **2021**, *11* (11). https://doi.org/10.3390/membranes11110822.

(30) Benmehel, A.; Chabab, S.; Do Nascimento Rocha, A. L.; Chepy, M.; Kousksou, T. PEM Water Electrolyzer Modeling: Issues and Reflections. *Energy Conversion and Management: X*. Elsevier Ltd October 1, 2024. https://doi.org/10.1016/j.ecmx.2024.100738.

(31) Liu, C.; Shviro, M.; Gago, A. S.; Zaccarine, S. F.; Bender, G.; Gazdzicki, P.; Morawietz, T.; Biswas, I.; Rasinski, M.; Everwand, A.; Schierholz, R.; Pfeilsticker, J.; Müller, M.; Lopes, P. P.; Eichel, R. A.; Pivovar, B.; Pylypenko, S.; Friedrich, K. A.; Lehnert, W.; Carmo, M. Exploring the Interface of Skin-Layered Titanium Fibers for Electrochemical Water Splitting. *Adv Energy Mater* **2021**, *11* (8). https://doi.org/10.1002/aenm.202002926.

(32) Feng, Q.; Yuan, X. Z.; Liu, G.; Wei, B.; Zhang, Z.; Li, H.; Wang, H. A Review of Proton Exchange Membrane Water Electrolysis on Degradation Mechanisms and Mitigation Strategies. *Journal of Power Sources*. Elsevier B.V. 2017, pp 33–55. https://doi.org/10.1016/j.jpowsour.2017.09.006.

(33) Frensch, S. H.; Fouda-Onana, F.; Serre, G.; Thoby, D.; Araya, S. S.; Kær, S. K. Influence of the Operation Mode on PEM Water Electrolysis Degradation. *Int J Hydrogen Energy* **2019**, *44* (57), 29889–29898.

(34) Rakousky, C.; Reimer, U.; Wippermann, K.; Kuhri, S.; Carmo, M.; Lueke, W.; Stolten, D. Polymer Electrolyte Membrane Water Electrolysis: Restraining Degradation in the Presence of Fluctuating Power. *J Power Sources* **2017**, *342*, 38–47. https://doi.org/10.1016/j.jpowsour.2016.11.118.

(35) Clarke, R. E.; Giddey, S.; Ciacchi, F. T.; Badwal, S. P. S.; Paul, B.; Andrews, J. Direct Coupling of an Electrolyser to a Solar PV System for Generating Hydrogen. *Int J Hydrogen Energy* **2009**, *34* (6), 2531–2542. https://doi.org/10.1016/j.ijhydene.2009.01.053.

(36) Wang, C. R.; Stansberry, J. M.; Mukundan, R.; Chang, H. M. J.; Kulkarni, D.; Park, A. M.; Plymill, A. B.; Firas, N. M.; Liu, C. P.; Lang, J. T.; Lee, J. K.; Tolouei, N. E.; Morimoto, Y.; Wang, C.; Zhu, G.; Brouwer, J.; Atanassov, P.; Capuano, C. B.; Mittelsteadt, C.; Peng, X.; Zenyuk, I. V. Proton Exchange Membrane (PEM) Water Electrolysis: Cell-Level Considerations for Gigawatt-Scale Deployment. *Chemical Reviews*. American Chemical Society February 12, 2025. https://doi.org/10.1021/acs.chemrev.3c00904.

(37) Grigoriev, S. A.; Bessarabov, D. G.; Fateev, V. N. Degradation Mechanisms of MEA Characteristics during Water Electrolysis in Solid Polymer Electrolyte Cells. *Russian Journal of Electrochemistry* **2017**, *53* (3), 318–323. https://doi.org/10.1134/S1023193517030065.

(38) Riaz, M. A.; Trogadas, P.; Aymé-Perrot, D.; Sachs, C.; Dubouis, N.; Girault, H.; Coppens, M. O. Water Electrolysis Technologies: The Importance of New Cell Designs and Fundamental Modelling to Guide Industrial-Scale Development. *Energy and Environmental Science*. Royal Society of Chemistry April 30, 2025. https://doi.org/10.1039/d4ee05559d.

(39) Bernt, M.; Schramm, C.; Schröter, J.; Gebauer, C.; Byrknes, J.; Eickes, C.; Gasteiger, H. A. Effect of the IrOx Conductivity on the Anode Electrode/Porous Transport Layer Interfacial Resistance in PEM Water Electrolyzers. *J Electrochem Soc* **2021**, *168* (8), 084513.

(40) Bernt, M.; Gasteiger, H. A. Influence of Ionomer Content in IrO2/TiO2 Electrodes on PEM Water Electrolyzer Performance. *J Electrochem Soc* **2016**, *163* (11), F3179.

(41) Trasatti, S. Physical Electrochemistry of Ceramic Oxides. *Electrochim Acta* **1991**, *36* (2), 225–241.

(42) Da Silva, L. A.; Alves, V. A.; Da Silva, M. A. P.; Trasatti, S.; Boodts, J. F. C. Oxygen Evolution in Acid Solution on IrO2+ TiO2 Ceramic Films. A Study by Impedance, Voltammetry and SEM. *Electrochim Acta* **1997**, *42* (2), 271–281.

(43) Gribov, E. N.; Kuznetsov, A. N.; Voropaev, I. N.; Golovin, V. A.; Simonov, P. A.; Romanenko, A. V.; Okunev, A. G. Analysis of the Corrosion Kinetic of Pt/C Catalysts Prepared on Different Carbon Supports under the "Start-Stop" Cycling. *Electrocatalysis* **2015**, *7* (2), 159–173. https://doi.org/10.1007/s12678-015-0294-6.

(44) Jensen, A. W.; Sievers, G. W.; Jensen, K. D.; Quinson, J.; Arminio-Ravelo, J. A.; Brüser, V.; Arenz, M.; Escudero-Escribano, M. Self-Supported Nanostructured Iridium-Based Networks as Highly Active Electrocatalysts for Oxygen Evolution in Acidic Media. *J Mater Chem A Mater* **2020**, *8* (3), 1066–1071.

(45) Lettenmeier, P.; Kolb, S.; Sata, N.; Fallisch, A.; Zielke, L.; Thiele, S.; Gago, A. S.; Friedrich, K. A. Comprehensive Investigation of Novel Pore-Graded Gas Diffusion Layers for High-Performance and Cost-Effective Proton Exchange Membrane Electrolyzers. *Energy Environ Sci* **2017**, *10* (12), 2521–2533. https://doi.org/10.1039/c7ee01240c.

(46) Travassos, M. A.; Lopes, V. V; Silva, R. A.; Novais, A. Q.; Rangel, C. M. Assessing Cell Polarity Reversal Degradation Phenomena in PEM Fuel Cells by Electrochemical Impedance Spectroscopy. *Int J Hydrogen Energy* **2013**, *38* (18), 7684–7696.

(47) Malevich, D.; Halliop, E.; Peppley, B. A.; Pharoah, J. G.; Karan, K. Investigation of Charge-Transfer and Mass-Transport Resistances in PEMFCs with Microporous Layer Using Electrochemical Impedance Spectroscopy. *J Electrochem Soc* **2008**, *156* (2), B216.

(48) Mueller, J. T.; Urban, P. M. Characterization of Direct Methanol Fuel Cells by Ac Impedance Spectroscopy. *J Power Sources* **1998**, *75* (1), 139–143.

(49) Antoine, O.; Bultel, Y.; Durand, R. Oxygen Reduction Reaction Kinetics and Mechanism on Platinum Nanoparticles inside Nafion®. *Journal of Electroanalytical Chemistry* **2001**, *499* (1), 85–94.

(50) Eikerling, M.; Kornyshev, A. A. Electrochemical Impedance of the Cathode Catalyst Layer in Polymer Electrolyte Fuel Cells. *Journal of Electroanalytical Chemistry* **1999**, *475* (2), 107–123.

(51) Bernt, M.; Schramm, C.; Schröter, J.; Gebauer, C.; Byrknes, J.; Eickes, C.; Gasteiger, H. A. Effect of the IrOx Conductivity on the Anode Electrode/Porous Transport Layer Interfacial Resistance in PEM Water Electrolyzers. *J Electrochem Soc* **2021**, *168* (8), 084513.

(52) Yadav, R.; Fedkiw, P. S. Analysis of EIS Technique and Nafion 117 Conductivity as a Function of Temperature and Relative Humidity. *J Electrochem Soc* **2012**, *159* (3), B340.

(53) Lettenmeier, P.; Kolb, S.; Sata, N.; Fallisch, A.; Zielke, L.; Thiele, S.; Gago, A. S.; Friedrich, K. A. Comprehensive Investigation of Novel Pore-Graded Gas Diffusion Layers for High-Performance and Cost-Effective Proton Exchange

Membrane Electrolyzers. *Energy Environ Sci* **2017**, *10* (12), 2521–2533. https://doi.org/10.1039/c7ee01240c.